

TENSILE PROPERTIES AND CORROSION BEHAVIOR OF BIODEGRADABLE IN SITU FORMED Mg–Si ALLOYS AND COMPOSITES

Mostafa Najafi, Hamed Mirzadeh , Rouhollah Mehdinavaz Aghdam and Massoud Emamy

School of Metallurgy and Materials Engineering, College of Engineering, University of Tehran, Tehran, Iran

Copyright © 2024 American Foundry Society
<https://doi.org/10.1007/s40962-024-01269-w>

Abstract

Tensile properties and in vitro corrosion behavior of biodegradable Mg–xSi alloys and composites in the simulated body fluid (SBF) solution were investigated. Besides pure magnesium, the hypoeutectic ($x = 0.1$ and 0.5 wt%), near-eutectic ($x = 1.2$ wt%), and hypereutectic ($x = 4$ wt%) compositions were considered. The Si addition in the hypoeutectic range resulted in the grain refinement of as-cast ingots, formation of α -Mg/Mg₂Si eutectic structure, and improvement of strength-ductility synergy. However, higher Si additions (1.2 and 4 wt%) led to poor tensile properties. Accordingly, the Mg–0.1Si and Mg–0.5Si alloys showed the best combination of tensile properties. The hot extrusion process resulted in a significant grain refinement induced by the dynamic recrystallization (DRX) and fragmentation of particles due to deformation, which led to a notable improvement of comprehensive tensile properties. For instance, the lean Mg–0.5Si alloy exhibited the highest

tensile toughness value of 37.3 MJ/m^3 , which is much larger than the value of 5.2 MJ/m^3 for the as-cast pure Mg. The extruded Mg–0.1Si sample showed the lowest corrosion current density (i_{Corr}) of $10 \mu\text{A/cm}^2$ in the SBF solution compared to other samples, which was ascribed to the fine grain size and formation of appropriate protective film with a high Ca/P ratio. However, higher Si additions resulted in the deterioration of corrosion resistance due to the increased amount of Mg₂Si phase. Accordingly, the Mg–0.1Si alloy was considered as a proper candidate for providing the best combination of tensile properties and corrosion resistance in biomedical implant applications.

Keywords: biomaterials, thermomechanical processing, grain refinement, mechanical properties, corrosion behavior

Introduction

In recent years, there has been a significant interest in the use of Mg alloys as potential biodegradable materials for bone implants because of their high strength, elastic modulus similar to bone tissue, and ability to degrade in the body.^{1–5} Many of the biodegradable Mg alloys are modifications of available alloys made for engineering purposes, which might not satisfy the requirements for biosafety and biocompatibility in biodegradable implant materials.^{6–9} Moreover, most currently researched Mg alloys degrade too quickly and experience a significant drop in strength during the initial stages of degradation, which poses a challenge for orthopedic biomaterials that require several months for bone healing and restoration of strength.^{10,11}

Silicon is a vital mineral in the human body, playing a crucial role in the healing process and immune system function.¹² It is also believed to be important for bone and connective tissue growth and development.¹³ Additionally, the presence of silicon in Mg alloys not only enhances the fluidity of the molten metal and aids in grain refinement, but also improves the hardness and decreases the corrosion current density.¹⁴ Therefore, there is potential for the use of Mg–Si alloys/composites as biodegradable bone implant materials. Besides, previous studies have shown that silicon is quite effective in improving the yield strength and ultimate tensile strength of pure Mg compared to other elements.^{15–17} Via addition of Si to Mg, the eutectic Mg₂Si phase in the hypoeutectic alloys and both primary and eutectic Mg₂Si phases in the hypereutectic alloys/composites appear by in situ reaction in the microstructure of the solidified alloy.¹⁸

However, the as-cast Mg–Si alloys/composites have shown low ductility and strength due to the presence of large Mg₂Si intermetallic particles and these particles accelerate the degradation rate of Mg–Si alloys/composites.^{19,20} Microstructural refinement by the addition of alloying elements or thermomechanical processing has been found to be an effective method for improving mechanical and corrosion properties.^{21–23} Thermomechanical processing is a widely used method to improve the properties of metallic alloys.^{24–26} Various hot deformation methods (such as extrusion, rolling, and forging) have been shown to refine the grain size of magnesium alloys through dynamic recrystallization (DRX).^{27–30} This process helps achieving a fine and homogeneous microstructure, which is beneficial for the performance of the material. For example, a study by Zhang et al.³¹ compared the corrosion properties of as-extruded and as-cast Mg–Nd–Zn–Zr alloy and found that the as-extruded alloy exhibited better corrosion resistance due to its refined and more homogenous microstructure. The second phase plays a significant role in promoting recrystallization during thermomechanical processing, resulting in a fine microstructure. Additionally, it can hinder grain growth through pinning or drag mechanisms during annealing treatment. Jiang and Yu³² reported a significant improvement of bio-corrosion resistance by using a gradient Mg–Si alloy, as compared with the traditional Mg–8 wt% Si alloy, which was ascribed to the compact and insoluble Mg₂Si phase distributed on the surface of the material.

Regarding Mg–Si alloys/composites, there has been a lack of comprehensive investigations on the tensile properties and bio-corrosion resistance at varying amounts of Si. As the amount of Si can significantly affect the microstructure and formation of phases, it should be optimized for obtaining the best combination of mechanical properties and corrosion resistance. Accordingly, the present study aims to fill this research gap by examining these properties in this specific scenario.

Experimental Details

Materials and Processing

The Mg–30 wt% Si master alloy and commercially pure Mg were utilized to create Mg–*x*Si alloys/composites, where *x* represents the weight percentage of Si and the *x* values are 0, 0.1, 0.5, 1.2, and 4, as also summarized in Table 1. Based on the binary Mg–Si phase diagram of Figure 1a, it can be seen that the eutectic composition and temperature are 1.34 wt% Si and 637.6 °C, respectively.³³ The Mg–0.1Si and Mg–0.5Si alloys are the hypoeutectic ones; the Mg–1.2Si alloy is near eutectic; while the Mg–4Si in situ composite is a hypereutectic alloy. Inside a graphite-ceramic crucible, the raw materials were melted in an induction furnace under the protection of a CO₂–5% SF₆

Table 1. Nominal Chemical Composition of the Studied Alloys

Alloy	Si content (wt%)	Alloy type
Pure Mg	0	Unalloyed pure metal
Mg–0.1Si	0.1	Hypoeutectic alloy
Mg–0.5Si	0.5	Hypoeutectic alloy
Mg–1.2Si	1.2	Near-eutectic alloy
Mg–4Si	4	Hypereutectic alloy

gas atmosphere. Prior to casting, the protecting gas was injected into the mold and the gas flow was also maintained during pouring. The molten alloys were then poured into a preheated uncoated metallic mold from a temperature of ~780 °C as determined by a K-type thermocouple, as shown in Figure 1b. Homogenization treatment was conducted at the temperature of 400 °C for 24 h to mitigate any chemical composition variations that may have arisen during the solidification process and to enhance the microstructure and morphology because of better material flow during the extrusion process. Subsequently, the hot extrusion process was conducted with an extrusion ratio of 1:12 (Figure 1c), following a 1 h soaking of the billet at 350 °C. These temperatures were selected based on the Mg–Si phase diagram and previous works on silicon-containing Mg alloys.^{34,35}

Characterization of Microstructure, Phases, and Tensile Behavior

The microstructures were revealed using a Olympus Vanox optical microscope with different magnifications from 40X to 1000X as well as a MIRA3 TESCAN scanning electron microscope (SEM) after etching with an acetic picral solution) 5 ml acetic acid, 6 g picric acid, 10 ml water, 100 ml ethanol(for 10 to 30 s. The average grain size was measured by the intercept method using image analysis method. Elemental analysis was performed using an energy dispersive spectroscopy (EDS) detector of the SEM instrument. Phase analysis was carried out using a PHILIPS X-ray diffractometer with Cu-K α radiation at a scan speed of 2°/min with a step interval of 0.5°. Room-temperature tensile tests were conducted on subsize ASTM E8 specimens with a gauge length of 16 mm (Figure 1d) using a cross-head speed of 0.1 mm/min (initial strain rate of 0.0001 s⁻¹). The tensile tests were repeated three times to ensure the reproducibility of the results. The strength-ductility balance was evaluated by the tensile toughness,³⁶ the area under the engineering stress (*S*)–engineering strain (*e*) curve, which was calculated using the trapezoidal rule expressed by $Area = \sum (e_i - e_{i-1})(S_i + S_{i-1})/2$.³⁷

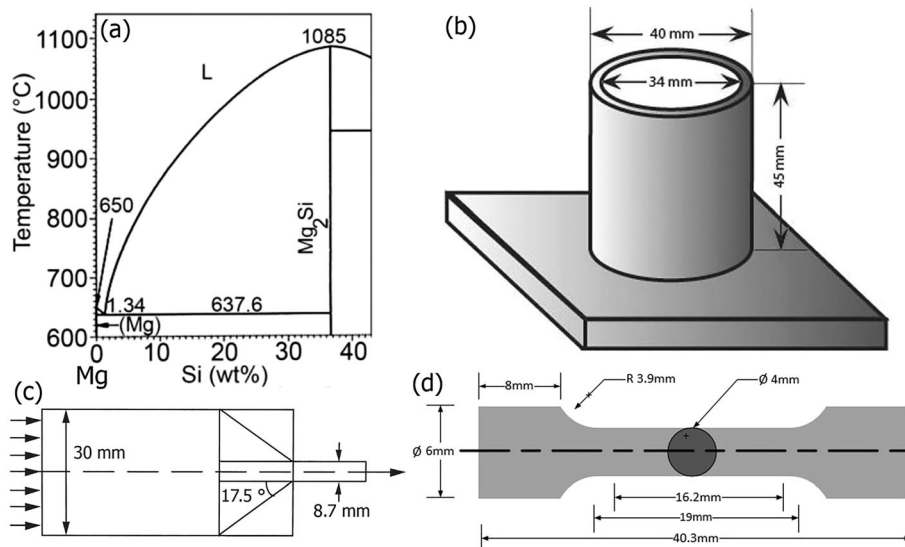


Figure 1. (a) Part of the binary Mg–Si phase diagram³³ as well as the schematic drawings of (b) mould, (c) extrusion process, and (d) tensile test specimen.

Corrosion Tests

For the electrochemical corrosion test, circular specimens were molded into epoxy resin, exposing only one side with an area of 60 mm^2 . The working surface was grind using SiC papers up to 1000 grit and then polished. The electrochemical test was performed at $37 \pm 1 \text{ }^\circ\text{C}$ ³⁸ in a beaker containing 100 ml of simulated body fluid (SBF) to stimulate the biological environment. A Solartron potentiostat (Model SI 1287) with a standard three-electrode configuration was used, with a saturated calomel electrode as the reference, a platinum electrode as the counter, and the sample as the working electrode. In the potentiodynamic polarization test, the working electrode was initially immersed in the simulated body fluid solution for 5 min, followed by the measurement of the polarization curve using the potential range of $\text{OCP} \pm 200 \text{ mV}$ at a scanning rate of 0.5 mV/s . After the test, SEM was used to inspect the surface of the samples. Moreover, surface elemental analysis was determined through the EDS detector.

Results and Discussion

Microstructures and Phases of As-Cast and Extruded Alloys

Figure 2 presents the optical and SEM images obtained for both pure Mg and Mg–Si alloys/composites in the as-cast state. Figure 3 presents the corresponding XRD results. The microstructure of pure Mg in Figure 2a exhibits a coarse grain size, averaging $520 \mu\text{m}$; while its XRD pattern in Figure 3 confirms the presence of $\alpha\text{-Mg}$ phase, as expected. Upon the addition of $0.1 \text{ wt}\%$ Si, a significant grain refinement with an average grain size of $63 \mu\text{m}$ was achieved, as shown in Figure 2b. During solidification,

grain refinement is related to the rate of development of growth restriction (Q) generated by the alloy chemistry, which establishes the constitutional undercooling needed to trigger nucleation events and facilitates their survival.^{39,40} According to previous research,⁴¹ the presence of a growth restriction factor of $Q = 9.25$ suggests that silicon is expected to exhibit a high degree of segregation in magnesium, resulting in a notable refinement of grain structure in the as-cast Mg alloys. Nelson⁴² further supports this notion, reporting that the addition of a small quantity of silicon to Mg alloys results in a significant grain refinement. Additionally, the presence of a second phase,²² namely Mg_2Si , is observable in Figure 2b and in the corresponding SEM image (Figure 2c) and XRD pattern (Figure 3). The needle-shaped morphology of this phase is related to the presence of this phase in the eutectic structure in this hypoeutectic alloy, as can be confirmed based on the binary Mg–Si phase diagram.

As shown in Figure 2d and e, the increase of $0.5 \text{ wt}\%$ Si further reduced the average grain size to $45 \mu\text{m}$, indicating a continued decrease compared to the change observed with the addition of 0.1% Si. Moreover, the eutectic $\alpha\text{-Mg}/\text{Mg}_2\text{Si}$ became more prominent and the needle-shaped morphology is more distinct. The increase in the amount of Mg_2Si phase can also be confirmed based on the increase in the peak intensities of Mg_2Si in the XRD pattern of Figure 3. As the percentage of Si approaches the eutectic composition, the proportion of the Mg_2Si increases (Figures 2f, g, and 3 for the Mg–1.2Si alloy) and the layered and eutectic morphology becomes more prominent. Beyond the eutectic point (in the hypereutectic range), the primary Mg_2Si phase in the microstructure of the Mg–4Si in situ composite, which resembles a Chinese script shape^{43,44} (Figure 2h and i for the Mg–4Si in situ composite), is formed adjacent to the eutectic layered structure.

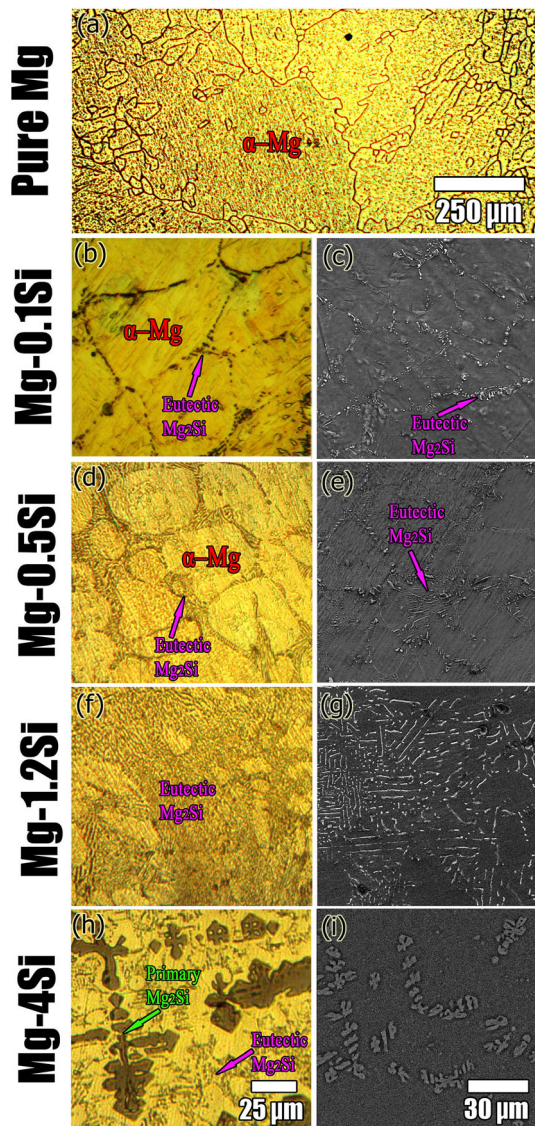


Figure 2. Optical and SEM images of pure Mg and as-cast Mg–Si binary alloys. The scale bars in parts (b), (d), (f), and (h) are same. Similarly, the scale bars in parts (c), (e), (g), and (i) are same.

The corresponding XRD diagram in Figure 3 demonstrates that the intensity of Mg_2Si peaks has increased while the intensity of α -Mg peaks has decreased.

Figure 4 illustrates the EDS point analysis conducted on the Mg–Si alloys/composites in both hypoeutectic and hypereutectic states. The weight and atomic percentages of silicon and magnesium in both states exhibit negligible variation, indicating the formation of Mg_2Si as the predominant composition. In fact, in both cases, the atomic ratio of Mg/Si is ~ 2 , which is consistent with the stoichiometry of the Mg_2Si phase.

Figure 5 presents the extruded microstructures of pure Mg and Mg–Si alloys/composites. The fragmentation of secondary phases^{45,46} and grain refinement by DRX^{47–49} can

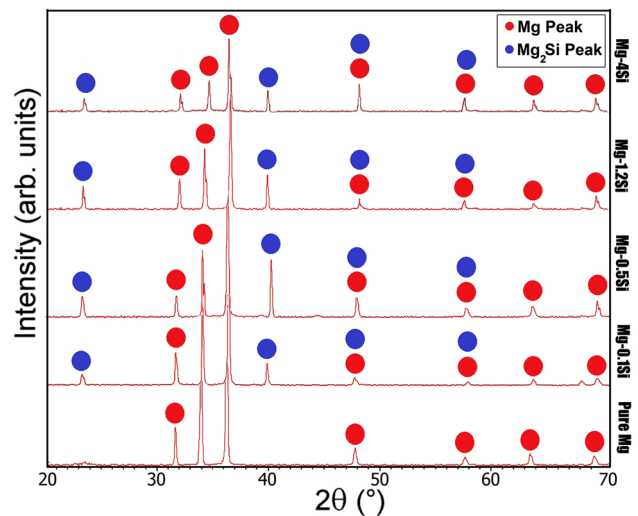


Figure 3. XRD patterns of pure Mg and as-cast Mg–Si binary alloys.

be seen in the provided micrographs, especially for the Mg–0.5Si alloy, where the average grain size of $11.7 \mu m$ was obtained for this sample. The absence of elongated grains in the extruded microstructures alongside the substantial decrease in grain size indicates the occurrence of DRX caused by mechanical working at elevated temperatures, which resulted in the development of fine-grained equiaxed microstructures.^{50,51} The presence of fragmented mg_2Si particles can also stimulate DRX via particle stimulated nucleation (PSN) mechanism in Mg–Si alloys/composites.^{52–54} However, the lamellar Mg_2Si can be seen in the SEM image of the Mg–1.2Si alloy. Moreover, still large primary Mg_2Si particles can be the optical image of the Mg–4Si in situ composite. These might significantly affect the tensile properties, as will be discussed in the following section.

Tensile Properties of As-Cast and Extruded Alloys

Figure 6a illustrates the tensile test results and changes in the tensile properties of as-cast alloys. The yield stress (YS) and ultimate tensile strength (UTS) of pure Mg are measured as 27 MPa and 98 MPa, respectively. However, the addition of 0.5 wt% silicon allows for the attainment of significantly higher values, reaching 58 MPa and 172 MPa, respectively. This doubling of strength levels does not come at the expense of a substantial decrease in the total elongation, as the percentage decreases from 7.5% for pure Mg to 5.8% for the Mg–0.5Si alloy. By comparing the tensile stress-strain curves of the hypoeutectic alloys (Mg, Mg–0.1Si, and Mg–0.5Si alloys), it is evident that an increase in Si content leads to an enhancement in strength and retaining good ductility. Conversely, the near eutectic alloy (Mg–1.2Si alloy) exhibits a decrease in UTS to 152 MPa. More importantly, as shown in Figure 6a, the

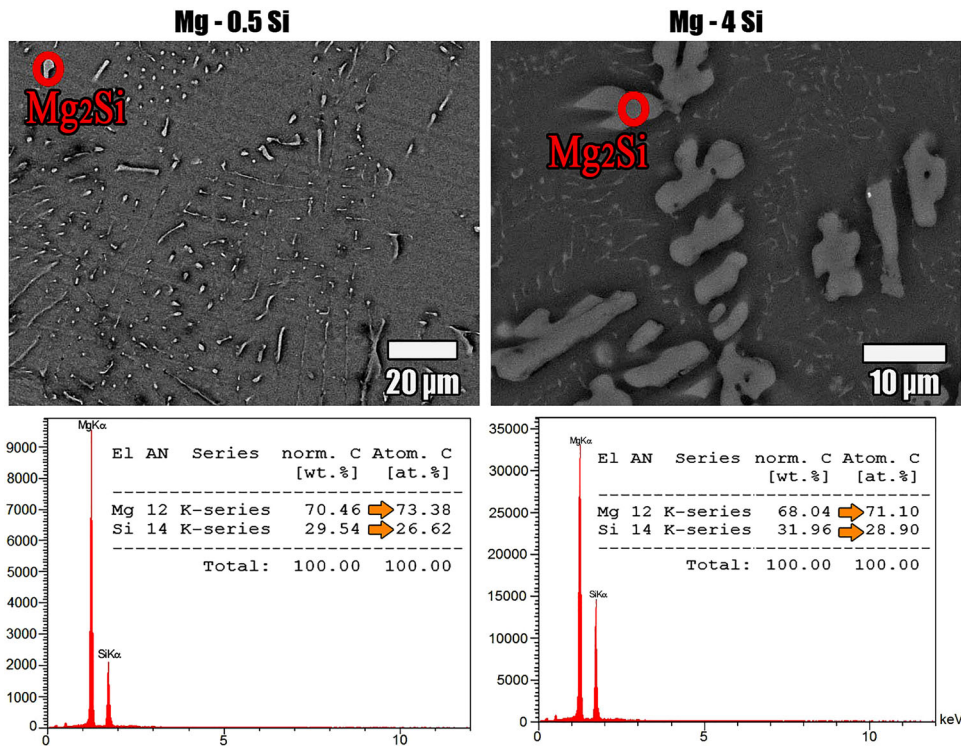


Figure 4. EDS analysis results of Mg-0.5Si alloy and Mg-4Si in situ composite.

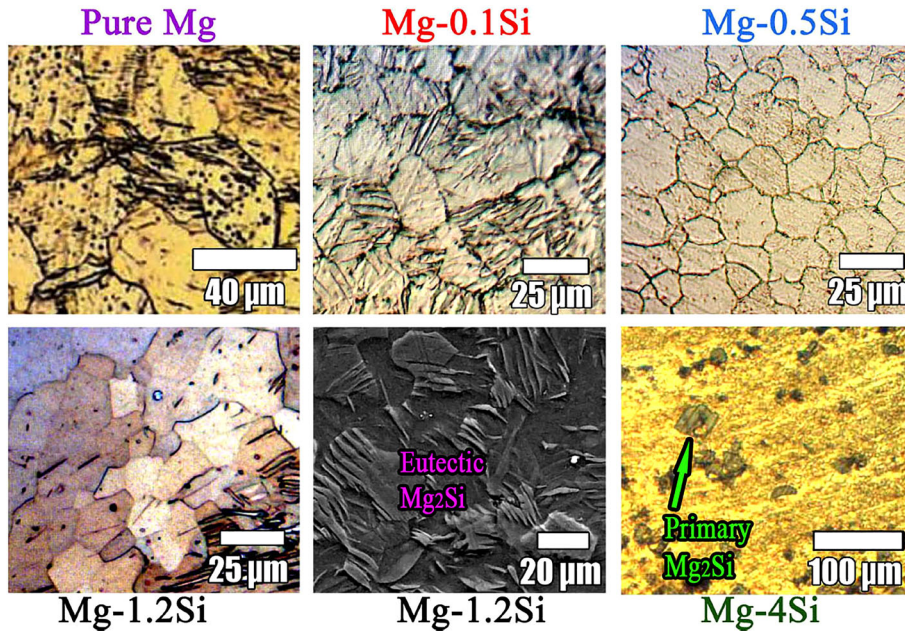


Figure 5. Microstructures of extruded alloys.

deterioration of tensile properties is particularly pronounced in terms of ductility, where the total elongation is nearly half that of the Mg-0.5Si alloy. Beyond the eutectic point, a transition of the background phase from the primary Mg to the primary Mg_2Si phase can be seen for the hypereutectic Mg-4Si in situ composite (Figure 2h). This alteration in the composition leads to the worsening of the brittleness of the hypereutectic Mg-4Si in situ composite.

The increased brittleness can be attributed not only to the more prominent presence of the Mg_2Si brittle phase but also to the morphology of the primary Mg_2Si particle, i.e., coarse dendritic primary Mg_2Si Chinese script type structures, which further contributes to the brittleness.^{55,56}

Figure 6b depicts the summary of the as-cast tensile properties, which are also tabulated in Table 2. It can be

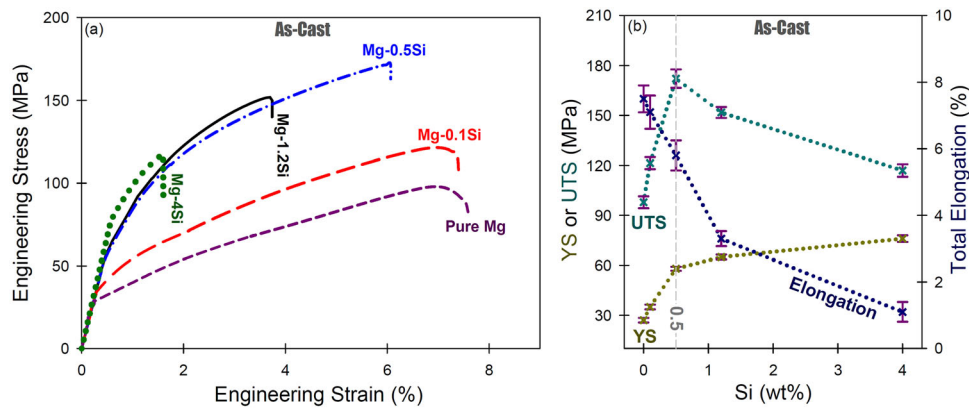


Figure 6. (a) Tensile stress–strain curves of the as-cast alloys and (b) summary of tensile properties.

Table 2. Summary of Tensile Properties for the As-Cast and Extruded Samples

Sample	As-Cast			As-Extruded		
	YS (MPa)	UTS (MPa)	Elongation (%)	YS (MPa)	UTS (MPa)	Elongation (%)
Pure Mg	27.1 ± 3	97.9 ± 3	7.5 ± 2	83 ± 2	193.3 ± 3	14.7 ± 2
Mg–0.1Si	34.7 ± 2	121.4 ± 4	7 ± 2	123.3 ± 3	234.5 ± 2	14.6 ± 2
Mg–0.5Si	57.6 ± 2	172.1 ± 3	5.8 ± 2	161.5 ± 3	266.1 ± 3	14.9 ± 2
Mg–1.2Si	64.8 ± 2	151.9 ± 2	3.3 ± 2	169.1 ± 2	250.5 ± 3	13.4 ± 3
Mg–4Si	75.7 ± 3	117.1 ± 3	1 ± 1	162 ± 3	212.4 ± 2	5.1 ± 2

seen that the optimization of alloy composition is quite important, as also demonstrated by Zeng et al.⁵⁷ Moreover, the Mg–0.5Si alloy shows the best comprehensive tensile properties with high YS, and significantly higher UTS, but a small decrement of total elongation compared to pure Mg. Therefore, the micro-addition of Si in the hypoeutectic range (–0.5 wt%) is quite effective for the improvement of tensile properties via grain refinement of α -Mg and formation of small amounts of eutectic constituent next to the primary α -Mg phase.

Figure 7a presents the tensile stress-strain curves of the extruded alloys; while the tensile properties are also tabulated in Table 2. It is evident that the overall tensile properties have significantly improved when compared to the as-cast alloys (Figure 6), which manifested itself into a notable increase in strength and total elongation. This is related to the fragmentation of secondary phases and grain refinement by DRX, as can be seen in the provided micrographs in Figure 5, especially for the Mg–0.5Si alloy, where the average grain size of 11.7 μm was obtained for this sample. Along with the enhanced strength, the improvement of ductility via grain refinement can be achieved by the activation of secondary slip systems⁵⁸ as well as the fragmentation and dispersion of second-phase particles,^{59,60} especially the eutectic constituent in the Mg–Si alloys/composites. Therefore, grain refinement in Mg

alloys might have a clear advantage of breaking the conventional strength-ductility trade off.

On the other hand, the trend of tensile properties with increasing Si content in Figure 7b closely resembles that of the casting counterparts (Figure 6b), where the UTS is initially improved but subsequently decreased as the amount of Si increases; while the total elongation is high at low Si contents and rapidly decreases with increasing Si content to 1.2 wt% (near-eutectic alloy) and especially for the hypereutectic in situ composite (Mg–4Si). The extruded microstructures of Mg–1.2Si alloy and Mg–4Si in situ composite are shown in Figure 5, revealing the presence of lamellar Mg₂Si (see SEM image for the Mg–1.2Si alloy) and still large primary Mg₂Si phases (see the optical image for the Mg–4Si in situ composite), which are responsible for the deterioration of tensile properties compared to the lean-Si alloys such as Mg–0.5Si alloy. Therefore, the micro-addition of Si in the hypoeutectic range combined with the extrusion process is quite effective for the improvement of tensile properties.

This fact can be better evaluated by consideration of tensile toughness, i.e. the area under the stress-strain curve, as shown in Figure 8. It can be seen that the tensile toughness values for extruded alloys are much larger, indicating the high energy spent on plastic deformation of the extruded

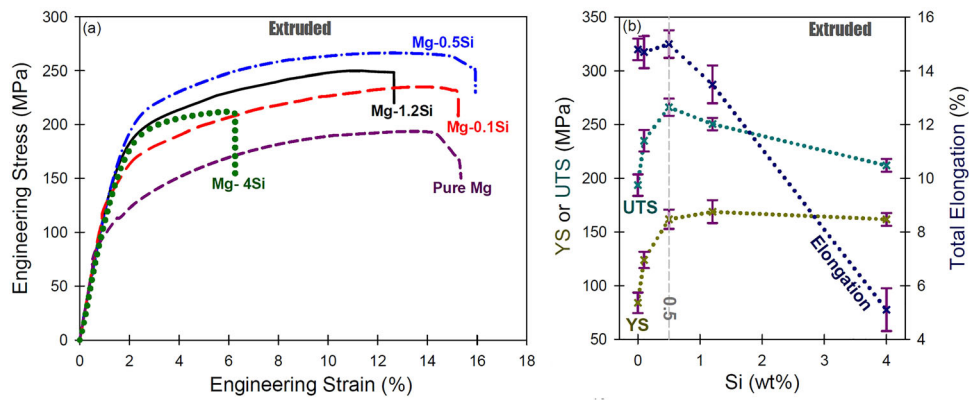


Figure 7. (a) Tensile stress–strain curves of the extruded alloys and (b) summary of tensile properties.

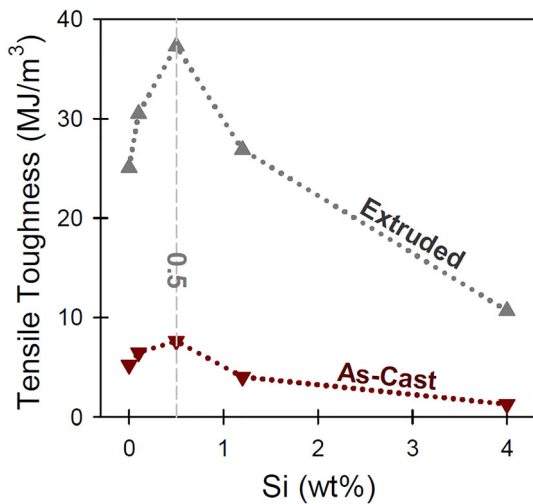


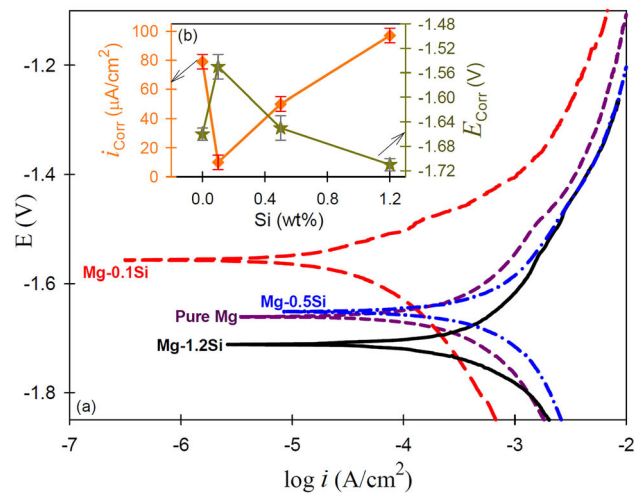
Figure 8. Calculated values of tensile toughness for the as-cast and extruded alloys.

alloys before fracturing. Moreover, among the extruded alloys, the lean Mg–0.5Si alloy exhibits the highest tensile toughness value of 37.3 MJ/m³, which is much larger compared to the value of 5.2 MJ/m³ for the as-cast pure Mg.

Corrosion Resistance of Extruded Alloys in the SBF Solution

Since the extruded alloys exhibited much better tensile properties compared to the as-cast counterparts, corrosion tests were performed on the extruded alloys to find the alloy with the best combination of tensile properties and corrosion resistance. Moreover, the Mg–4Si in situ composite was also neglected due to its poor tensile properties.

Figure 9a illustrates the polarization diagram for extruded pure Mg and Mg–Si alloys. Moreover, the relationship between corrosion current density (i_{corr}), corrosion potential (E_{corr}), and silicon content is depicted in Figure 9b. As



(c) Pure Mg Mg-0.1Si Mg-0.5Si Mg-1.2Si

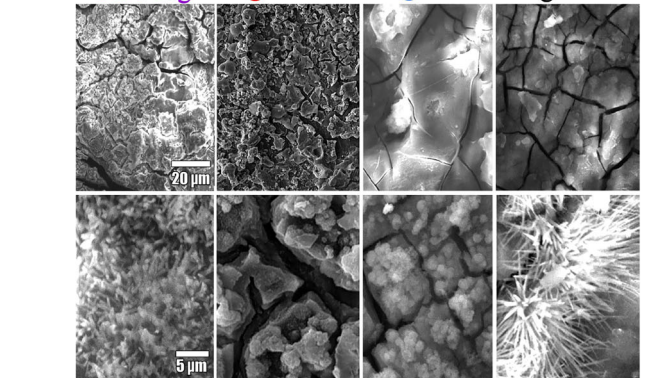


Figure 9. (a) Polarization curves of extruded Mg–Si alloys in SBF solution, (b) changes in i_{corr} and E_{corr} based on weight percentage of silicon, and (c) electron microscope images of the surface of Mg–Si alloys after the polarization test in SBF solution.

the silicon content increases to 0.1 wt%, there is an increase in E_{corr} and a decrease in i_{corr} . This suggests that the small addition of silicon has a favorable effect on the corrosion behavior of the alloys. The presence of silicon shifts the cathodic region of the polarization diagram, as also observed by Gusieva.⁶¹ Figure 9c depicts the surface

Table 3. Elemental Analysis of Corroded Surfaces of Extruded Mg–Si Alloys

Sample	Ca (wt%)	P (wt%)	Cl (wt%)	Molar ratio of Ca/P
Pure Mg	2.43	5.17	26.74	0.49
Mg–0.1Si	4.41	4.28	5.31	1.06
Mg0.5Si	3.87	5.35	27.27	0.74
Mg–1.2Si	8.62	13.06	28.80	0.68

morphology of the samples after corrosion, revealing some big cracks on the corroded surface of pure Mg. However, the surface appearance of the Mg–0.1Si alloy is much better.

Table 3 presents the results of EDS analysis from the surface of the corroded alloy, depicting the quantities of calcium, phosphorus, and chlorine, as well as their molar ratios on the surface of the samples. The low levels of calcium and phosphorus, with a Ca/P ratio of 0.49, indicate the presence of a weak corrosion film for pure Mg. This ratio is much lower than those observed in tricalcium-phosphate ($\text{Ca}_3(\text{PO}_4)_2$) and hydroxyapatite ($\text{Ca}_{10}(\text{PO}_4)_6(\text{OH})_2$), further supporting the notion of limited corrosion resistance. Conversely, a high Ca/P ratio implies a reduced dissolution rate and faster repair process,⁶² as is the case for the Mg–0.1Si alloy with a Ca/P ratio of 1.06 (Table 3). In fact, the fine grain size of Mg–0.1Si alloy (20.5 μm on average) with negligible effect of Mg_2Si due to its small amount is responsible for the improved corrosion resistance and formation of a more compact protective layer on the surface, which is an important aspect.⁶³

As depicted in Table 3, the Mg–0.5Si alloy exhibits a higher Ca/P ratio compared to pure Mg, although the value of 0.74 is still low. Electron microscopy image of the corroded surface of this alloy in Figure 9c reveals a more appropriate protective layer for this alloy compared to pure Mg. However, a high amount of chlorine can also be detected on the surface (Table 3), which is undesirable as it leads to the dissolution of the film and accelerates the corrosion process. Similar results are obtained for the Mg–1.2Si alloy, with even worse outcomes. The Ca/P ratio for this alloy is 0.68 (Table 3), lower than that of the Mg–0.5Si alloy. However, the morphology of the formed layer differs from pure magnesium, possibly due to the lower amount of Cl/(Ca,P) causing less destruction of the layer.

These results reveal that the presence of high amount of Mg_2Si is unfavorable. For pure Mg and Mg–1.2Si samples, the formed layer exhibits a needle-like morphology (Figure 9c), suggesting the early stages of calcium phosphate formation. However, in Mg–0.1Si and Mg–0.5Si samples, the morphology has evidently changed, indicating the

formation of a reliable protective surface layer. These results reveal that the Mg–0.1Si alloy shows the best corrosion resistance and the Mg–0.5Si alloy can be considered the second best one; while the corrosion resistance of pure Mg and Mg–1.2Si alloy is inferior.

In summary, by studying the extruded samples, the present work revealed that the Si content of 0.5 wt% is favorable to improve the strength-ductility synergy; while the improvements achieved at a low level of 0.1 wt% are also notable. However, regarding the corrosion resistance in the SBF solution, the Si content of 0.1 wt% was found to be quite effective for the improvement of this property; while other samples showed high corrosion current densities. Accordingly, the Mg–0.1Si alloy can be considered as the candidate of the best combination of tensile properties and corrosion resistance in the SBF solution for biomedical applications.

Conclusions

Tensile properties and in vitro corrosion behavior (in SBF solution) of biodegradable Mg–Si alloys/composites (Si in the range of 0 to 4 wt%) were investigated. The following conclusions can be drawn:

- (1) Si addition in the hypoeutectic range (0.1 and 0.5 wt%) resulted in the grain refinement of as-cast ingots, formation of eutectic Mg_2Si phase, and improvement of strength-ductility synergy. However, higher Si additions (1.2 and 4 wt%) led to poor tensile properties. Accordingly, the Mg–0.1Si and Mg–0.5Si alloys showed the best combination of tensile properties.
- (2) A notable improvement of comprehensive tensile properties after hot extrusion was observed. For instance, the lean Mg–0.5Si alloy exhibited the highest tensile toughness value of 37.3 MJ/m³, which is much larger than the value of 5.2 MJ/m³ for the as-cast pure Mg.
- (3) The extruded Mg–0.1Si sample showed the lowest corrosion current density in the SBF solution compared to other samples. For instance, i_{CORR} values of 10 and 79 $\mu\text{A}/\text{cm}^2$ were obtained for the extruded Mg–0.1Si and pure Mg samples, respectively. However, higher Si additions resulted in the deterioration of corrosion resistance. For instance, i_{CORR} values of 50 and 97 $\mu\text{A}/\text{cm}^2$ were obtained for the extruded Mg–1.2Si alloy and Mg–4Si in situ composite, respectively.
- (4) The Mg–0.1Si alloy was considered as the candidate of best combination of tensile properties and corrosion resistance in biomedical applications.

Funding

This work received no funding.

Data Availability

The authors stated that the processed data required to reproduce these findings were available in this manuscript.

Conflict of interest The authors declare no conflict of interest.

Ethical Approval The manuscript has been prepared by the contribution of all authors, it is the original authors work, it has not been published before, it has been solely submitted to this journal, and if accepted, it will not be submitted to any other journal in any language.

REFERENCES

1. D. Bairagi, S. Mandal, A comprehensive review on biocompatible Mg-based alloys as temporary orthopaedic implants: current status, challenges, and future prospects. *J. Magnes. Alloy* **10**, 627–669 (2022). <https://doi.org/10.1016/j.jma.2021.09.005>
2. H. Zengin, Role of Sr in microstructure, hardness and biodegradable behavior of cast Mg–2Zn–2Ca–0.5 Mn (ZXM220) alloy for potential implant application. *Int. J. Met.* **14**, 442–453 (2020). <https://doi.org/10.1007/s40962-019-00366-5>
3. P. Vignesh, S. Ramanathan, M. Ashokkumar, T. Sonar, V. Ananthi, Microstructure, mechanical, and electrochemical corrosion performance of Ti/HA (Hydroxyapatite) particles reinforced Mg–3Zn squeeze casted composites. *Int. J. Met.* (2023). <https://doi.org/10.1007/s40962-023-01114-6>
4. B. Cicek, L. Elen, E. Koc, A.N. Saud, Y. Sun, Investigation of intermetallic phase fractions and dry-corrosive wear properties in Mg–Al–Si ternary alloy. *Int. J. Met.* (2023). <https://doi.org/10.1007/s40962-023-00992-0>
5. Z. Savaedi, H. Mirzadeh, R.M. Aghdam, R. Mahmudi, Effect of grain size on the mechanical properties and bio-corrosion resistance of pure magnesium. *J. Mater. Res. Technol.* **19**, 3100–3109 (2022). <https://doi.org/10.1016/j.jmrt.2022.06.048>
6. Z. Savaedi, R. Motallebi, H. Mirzadeh, R.M. Aghdam, R. Mahmudi, Superplasticity of fine-grained magnesium alloys for biomedical applications: a comprehensive review. *Curr. Opin. Solid State Mater. Sci.* **27**, 101058 (2023). <https://doi.org/10.1016/j.cossms.2023.101058>
7. M.T. Colomina, F. Peris-Sampedro, Aluminum and Alzheimer's disease. *Neurotox. Met.* (2017). https://doi.org/10.1007/978-3-319-60189-2_9
8. Y. Yang, X. Xiong, J. Chen, X. Peng, D. Chen, F. Pan, Research advances of magnesium and magnesium alloys worldwide in 2022. *J. Magnes. Alloys*. **11**, 2611–2654 (2023). <https://doi.org/10.1016/j.jma.2023.07.011>
9. K.T. Rim, Effects of rare earth elements on the environment and human health: a literature review. *J. Toxicol. Environ. Health Sci.* **8**, 189–200 (2016). <https://doi.org/10.1007/s13530-016-0276-y>
10. S. Zhang, X. Zhang, C. Zhao, J. Li, Y. Song, C. Xie, H. Tao, Y. Zhang, Y. He, Y. Jiang, Y. Bian, Research on an Mg–Zn alloy as a degradable biomaterial. *Acta Biomater.* **6**, 626–640 (2010). <https://doi.org/10.1016/j.actbio.2009.06.028>
11. Z. Savaedi, H. Mirzadeh, R.M. Aghdam, R. Mahmudi, Thermal stability, grain growth kinetics, mechanical properties, and bio-corrosion resistance of pure Mg, ZK30, and ZEK300 alloys: a comparative study. *Mater. Today Commun.* **33**, 104825 (2022). <https://doi.org/10.1016/j.mtcomm.2022.104825>
12. E. Zhang, L. Yang, J. Xu, H. Chen, Microstructure, mechanical properties and bio-corrosion properties of Mg–Si (–Ca, Zn) alloy for biomedical application. *Acta Biomater.* **6**, 1756–1762 (2010). <https://doi.org/10.1016/j.actbio.2009.11.024>
13. S. Sripanyakorn, R. Jugdaohsingh, H. Elliott, C. Walker, P. Mehta, S. Shoukru, R.P. Thompson, J.J. Powell, The silicon content of beer and its bioavailability in healthy volunteers. *Br. J. Nutr.* **91**, 403–409 (2004). <https://doi.org/10.1079/BJN20031082>
14. W. Wang, M. Gao, Y. Huang, L. Tan, K. Yang, N. Hort, Microstructures, corrosion and mechanical properties of Mg–Si alloys as biodegradable implant materials. *Magnes. Technol.* (2019). https://doi.org/10.1007/978-3-030-05789-3_23
15. Y.F. Zheng, X.N. Gu, F. Witte, Biodegradable metals. *Mater. Sci. Eng. R. Rep.* **77**, 1–34 (2014). <https://doi.org/10.1016/j.mser.2014.01.001>
16. X. Gu, Y. Zheng, Y. Cheng, S. Zhong, T. Xi, In vitro corrosion and biocompatibility of binary magnesium alloys. *Biomaterials* **30**(4), 484–498 (2009). <https://doi.org/10.1016/j.biomaterials.2008.10.021>
17. A.R. Salasel, A. Abbasi, N. Barri, H. Mirzadeh, M. Emamy, M. Malekan, Effect of Si and Ni on microstructure and mechanical properties of in-situ magnesium-based composites in the as-cast and extruded conditions. *Mater. Chem. Phys.* **232**, 305–310 (2019). <https://doi.org/10.1016/j.matchemphys.2019.04.079>
18. A. Malik, Y. Wang, A short review on high strain rate superplasticity in magnesium-based composites materials. *Int. J. Lightweight Mater. Manuf.* **6**(2), 214–224 (2023). <https://doi.org/10.1016/j.ijlmm.2022.10.004>
19. N. Hort, Y.D. Huang, K.U. Kainer, Intermetallics in magnesium alloys. *Adv. Eng. Mater.* **8**(4), 235–240 (2006). <https://doi.org/10.1002/adem.200500202>
20. E. Zhang, X. Wei, L. Yang, J. Xu, C. Song, Effect of Zn on the microstructure and mechanical properties of Mg–Si alloy. *Mater. Sci. Eng. A* **527**(13–14),

- 3195–3199 (2010). <https://doi.org/10.1016/j.msea.2010.01.074>
21. M. Maleki, H. Mirzadeh, M. Emamy, Improvement of mechanical properties of in situ Mg–Si composites via Cu addition and hot working. *J. Alloys Compd.* **905**, 164–176 (2022). <https://doi.org/10.1016/j.jallcom.2022.164176>
 22. M. Jamalpour, R. Alizadeh, Effects of heat treatment and Y addition on the microstructure and mechanical properties of as-cast Mg–Si alloys. *Mater. Sci. Eng. A* **859**, 144209 (2022). <https://doi.org/10.1016/j.msea.2022.144209>
 23. M. Golrang, M. Mobasheri, H. Mirzadeh, M. Emamy, Effect of Zn addition on the microstructure and mechanical properties of Mg–0.5Ca–0.5 RE magnesium alloy. *J. Alloys Compd.* **815**, 152380 (2020). <https://doi.org/10.1016/j.jallcom.2019.152380>
 24. A. Rollett, G.S. Rohrer, J. Humphreys, *Recrystallization and Related Annealing Phenomena* (Elsevier, Amsterdam, 2017)
 25. A.H. Shafieizad, A. Zarei-Hanzaki, H.R. Abedi, K.J. Al-Fadhalah, The Mg₂Si phase evolution during thermomechanical processing of in-situ aluminum matrix macro-composite. *Mater. Sci. Eng. A* **644**, 310–317 (2015). <https://doi.org/10.1016/j.msea.2015.07.060>
 26. M. Roostaei, M.H. Parsa, R. Mahmudi, H. Mirzadeh, Hot compression behavior of GZ31 magnesium alloy. *J. Alloys Compd.* **631**, 1–6 (2015). <https://doi.org/10.1016/j.jallcom.2014.11.188>
 27. H. Mirzadeh, Grain refinement of magnesium alloys by dynamic recrystallization (DRX): a review. *J. Mater. Res. Technol.* **25**, 7050–7077 (2023). <https://doi.org/10.1016/j.jmrt.2023.07.150>
 28. Y. Deng, H. Yan, Q. Li, J. Chen, W. Xia, B. Su, M. Wu, Y. Yu, M. Song, Enhancing strength and ductility of low RE content Mg–Gd–Y–Zr alloy via a novel thermomechanical treatment based on multi-directional forging. *J. Alloys Compd.* **958**, 170535 (2023). <https://doi.org/10.1016/j.jallcom.2023.170535>
 29. S.M. Fatemi-Varzaneh, A. Zarei-Hanzaki, J.M. Cabrera, P.R. Calvillo, EBSD characterization of repetitive grain refinement in AZ31 magnesium alloy. *Mater. Chem. Phys.* **149**, 339–343 (2015). <https://doi.org/10.1016/j.matchemphys.2014.10.026>
 30. M.S. Mehranpour, A. Heydarinia, M. Emamy, H. Mirzadeh, A. Koushki, R. Razi, Enhanced mechanical properties of AZ91 magnesium alloy by inoculation and hot deformation. *Mater. Sci. Eng. A* **802**, 140667 (2021). <https://doi.org/10.1016/j.msea.2020.140667>
 31. X. Zhang, G. Yuan, Z. Wang, Mechanical properties and biocorrosion resistance of Mg–NdZn–Zr alloy improved by cyclic extrusion and compression. *Mater. Lett.* **74**, 128–131 (2012). <https://doi.org/10.1016/j.matlet.2012.01.086>
 32. W. Jiang, W. Yu, Corrosion behavior and osteogenic activity of a biodegradable orthopedic implant Mg–Si alloy with a gradient structure. *Metals* **11**, 781 (2021). <https://doi.org/10.3390/met11050781>
 33. H. Okamoto, H. Okamoto, *Phase Diagrams for Binary Alloys* (ASM international, Detroit, 2000)
 34. L. Zhang, J. Wang, Y. Zhu, B. Shi, P. Jin, Hot deformation behaviors and microstructure evolution of Mg–Si–Sr alloy. *Mater. Res. Express* **7**(9), 096502 (2020). <https://doi.org/10.1088/2053-1591/abb153>
 35. Z. Zeng, N. Stanford, C.H.J. Davies, J.F. Nie, N. Birbilis, Magnesium extrusion alloys: a review of developments and prospects. *Int. Mater. Rev.* **64**(1), 27–62 (2019). <https://doi.org/10.1080/09506608.2017.1421439>
 36. M.J. Sohrabi, H. Mirzadeh, S. Sadeghpour, R. Mahmudi, Grain size dependent mechanical behavior and TRIP effect in a metastable austenitic stainless steel. *Int. J. Plast.* **160**, 103502 (2023). <https://doi.org/10.1016/j.ijplas.2022.103502>
 37. M.R. Moazami, A. Razaghian, H. Mirzadeh, M. Emamy, Tailoring the mechanical properties of hypereutectic in situ Al–Mg₂Si composites via hybrid TiB₂ reinforcement and hot extrusion. *Arch. Civ. Mech.* **22**, 87 (2022). <https://doi.org/10.1007/s43452-022-00416-6>
 38. U. Masood Chaudry, A. Farooq, A. Malik, M. Nabeel, M. Sufyan, A. Tayyeb, S. Asif, A. Inam, A. Elbalaawy, E. Hafez, T.S. Jun, Biodegradable properties of AZ31–0.5Ca magnesium alloy. *Mater. Technol.* **37**, 2230–2241 (2022). <https://doi.org/10.1080/10667857.2021.2022571>
 39. M.A. Easton, M. Qian, A. Prasad, D.H. StJohn, Recent advances in grain refinement of light metals and alloys. *Curr. Opin. Solid State Mater. Sci.* **20**, 13–24 (2016). <https://doi.org/10.1016/j.cossms.2015.10.001>
 40. M. Emamy, H. Mirzadeh, M. Ra'ayatpour, H. Abedi, Mechanical properties of as-cast and wrought Mg–5Ni–xAl magnesium alloys. *Mater. Sci. Eng. A* **840**, 142996 (2022). <https://doi.org/10.1016/j.msea.2022.142996>
 41. D.H. StJohn, M.A. Qian, M.A. Easton, P. Cao, Z. Hildebrand, Grain refinement of magnesium alloys. *Metall. Mater. Trans. A* **36**, 1669–1679 (2005). <https://doi.org/10.1007/s11661-005-0030-6>
 42. C.E. Nelson, Grain size behavior in magnesium casting alloys. *Trans. AFS* **56**, 1–23 (1948)
 43. K.K. Ajith Kumar, A. Srinivasan, U.T.S. Pillai, B.C. Pai, M. Chakraborty, Microstructure and mechanical property correlation of Mg–Si alloys. *Silicon* **14**(15), 9499–9515 (2022). <https://doi.org/10.1007/s12633-021-01521-6>
 44. Y. Pan, X. Liu, H. Yang, Microstructural formation in a hypereutectic Mg–Si alloy. *Mater Charact* **55**(3), 241–247 (2005). <https://doi.org/10.1016/j.matchar.2005.07.009>
 45. J. Metayer, Y.E. Bing, G.U.O. Wei, Q.D. Wang, Z.H.O.U. Hao, F. Mollet, Microstructure and mechanical properties of Mg–Si alloys processed by cyclic closed-die forging. *Trans. Nonferrous Met. Soc.*

- China **24**(1), 66–75 (2014). [https://doi.org/10.1016/S1003-6326\(14\)63029-6](https://doi.org/10.1016/S1003-6326(14)63029-6)
46. D. Zhang, Q. Yang, K. Guan, B. Li, N. Wang, P. Qin, B. Jiang, C. Sun, X. Qin, Z. Tian, Z. Cao, A high-strength low-rare-earth-alloyed magnesium alloy via traditional hot-extrusion. *J. Alloys Compd.* **810**, 151967 (2019). <https://doi.org/10.1016/j.jallcom.2019.151967>
 47. Ö. Ayer, Effect of die parameters on the grain size, mechanical properties and fracture mechanism of extruded AZ31 magnesium alloys. *Mater. Sci. Eng. A* **793**, 139887 (2020). <https://doi.org/10.1016/j.msea.2020.139887>
 48. M.S. Geshani, P.M. Kalayeh, A.H. Asadi, H. Mirzadeh, M. Malekan, M. Emamy, A review of Mg alloys containing long-period stacking ordered (LPSO) structures with insight into the application of friction stir processing. *J. Mater. Res. Technol.* **24**, 4945–4966 (2023). <https://doi.org/10.1016/j.jmrt.2023.04.105>
 49. I. Dinaharan, S. Zhang, G. Chen, Q. Shi, Assessment of Ti–6Al–4V particles as a reinforcement for AZ31 magnesium alloy-based composites to boost ductility incorporated through friction stir processing. *J. Magnes. Alloy.* **10**(4), 979–992 (2022). <https://doi.org/10.1016/j.jma.2020.09.026>
 50. K.E. Huang, R.E. Logé, A review of dynamic recrystallization phenomena in metallic materials. *Mater. Des.* **111**, 548–574 (2016). <https://doi.org/10.1016/j.matdes.2016.09.012>
 51. T. Sakai, A. Belyakov, R. Kaibyshev, H. Miura, J.J. Jonas, Dynamic and post-dynamic recrystallization under hot, cold and severe plastic deformation conditions. *Prog. Mater. Sci.* **60**, 130–207 (2014). <https://doi.org/10.1016/j.pmatsci.2013.09.002>
 52. M. Lotfipour, A. Bahmani, H. Mirzadeh, M. Emamy, M. Malekan, W.J. Kim, M. Taghizadeh, A. Afsharnaderi, Effect of microalloying by Ca on the microstructure and mechanical properties of as-cast and wrought Mg–Mg₂Si composites. *Mater. Sci. Eng. A* **820**, 141574 (2021). <https://doi.org/10.1016/j.msea.2021.141574>
 53. L.P. Troeger, E.A. Starke Jr., Particle-stimulated nucleation of recrystallization for grain-size control and superplasticity in an Al–Mg–Si–Cu alloy. *Mater. Sci. Eng. A* **293**, 19–29 (2000). [https://doi.org/10.1016/S0921-5093\(00\)01235-1](https://doi.org/10.1016/S0921-5093(00)01235-1)
 54. M. Rezayat, M.H. Parsa, H. Mirzadeh, J.M. Cabrera, Texture development during hot deformation of Al/Mg alloy reinforced with ceramic particles. *J. Alloys Compd.* **798**, 267–272 (2019). <https://doi.org/10.1016/j.jallcom.2019.05.233>
 55. G.L. de Gouveia, A. Garcia, J.E. Spinelli, Tailoring microstructure and tensile properties of Mg–Si alloys varying solidification cooling rate and Si content. *Mater. Sci. Eng. A* **825**, 141905 (2021). <https://doi.org/10.1016/j.msea.2021.141905>
 56. X.S. Hu, K. Wu, M.Y. Zheng, W.M. Gan, X.J. Wang, Low frequency damping capacities and mechanical properties of Mg–Si alloys. *Mater. Sci. Eng. A* **452**, 374–379 (2007). <https://doi.org/10.1016/j.msea.2006.10.099>
 57. Z. Zeng, M. Bian, S. Xu, W. Tang, C. Davies, N. Birbilis, J. Nie, Optimisation of alloy composition for highly-formable magnesium sheet. *Int. J. Miner. Metall. Mater.* **29**, 1388–1395 (2022). <https://doi.org/10.1007/s12613-021-2365-4>
 58. K. Wei, R. Hu, D. Yin, L. Xiao, S. Pang, Y. Cao, H. Zhou, Y. Zhao, Y. Zhu, Grain size effect on tensile properties and slip systems of pure magnesium. *Acta Mater.* **206**, 116604 (2021). <https://doi.org/10.1016/j.actamat.2020.116604>
 59. A. Afsharnaderi, M. Lotfipour, H. Mirzadeh, M. Emamy, M. Malekan, Enhanced mechanical properties of as-cast AZ91 magnesium alloy by combined RE–Sr addition and hot extrusion. *Mater. Sci. Eng. A* **792**, 139817 (2020). <https://doi.org/10.1016/j.msea.2020.139817>
 60. H. Huang, H. Liu, C. Wang, J. Sun, J. Bai, F. Xue, J. Jiang, A. Ma, Potential of multi-pass ECAP on improving the mechanical properties of a high-calcium-content Mg–Al–Ca–Mn alloy. *J. Magnes. Alloys* **7**, 617–627 (2019). <https://doi.org/10.1016/j.jma.2019.04.008>
 61. K. Gusieva, C.H.J. Davies, J.R. Scully, N. Birbilis, Corrosion of magnesium alloys: the role of alloying. *Int. Mater. Rev.* **60**(3), 169–194 (2015). <https://doi.org/10.1179/1743280414Y.0000000046>
 62. F. Ghorbani, H. Mirzadeh, C. Dehghanian, M. Emamy, Mechanical properties and corrosion behavior of biodegradable Mg–0.5 Zr–0.5 Ca–xZn magnesium alloys. *Adv. Eng. Mater.* **25**(10), 2201778 (2023). <https://doi.org/10.1002/adem.202201778>
 63. E. Gerashi, M. Jamalpour, R. Alizadeh, S. Labbaf, R. Mahmudi, Effects of hydrothermal coating on the degradation behavior and biocompatibility of an Mg–4Zn–0.3Sr alloy. *Mater. Lett.* **330**, 133224 (2023). <https://doi.org/10.1016/j.matlet.2022.133224>

Publisher’s Note Springer Nature remains neutral with regard to jurisdictional claims in published maps and institutional affiliations.

Springer Nature or its licensor (e.g. a society or other partner) holds exclusive rights to this article under a publishing agreement with the author(s) or other rightsholder(s); author self-archiving of the accepted manuscript version of this article is solely governed by the terms of such publishing agreement and applicable law.